Small-angle scattering indicates equilibrium instead of metastable capillary condensation in SBA-15 mesoporous silica

Ali F. Haidar,[†] Artium Belet,[†] Bart Goderis,[‡] Alexandre F. Léonard,[¶] and Cedric J. Gommes[*,†]

[†]*Department of Chemical Engineering, University of Liège B6A, Allée du Six Août 3, B-4000 Liège, Belgium*

[‡]*Polymer Chemistry and Materials, KU Leuven, Celestijnenlaan 200F, Leuven, B-3001, Belgium*

[¶]*CARPOR - Department of Chemical Engineering, University of Liège B6A, Allée du Six Août 3, B-4000 Liège, Belgium*

E-mail: cedric.gommes@uliege.be

Abstract

Questions about the origin of the adsorption/desorption hysteresis in mesoporous materials are as old as sorption experiments themselves. The historical conception that underlines most existing methods to extract pore size distributions from sorption data, assumes that adsorption is a metastable process and that desorption takes place at thermodynamic equilibrium. In this work, we measure nitrogen and argon sorption on a series of fourteen SBA-15 ordered mesoporous silicas, and we use small-angle x-ray scattering to independently determine their pore sizes. We find that capillary condensation systematically occurs close to thermodynamic equilibrium according to

a Derjaguin-Broekhoff-de Boer calculation. Our analysis suggests that many earlier works have significantly underestimated the actual pore size in SBA-15 materials. It also highlights the critical role of the reference isotherm used to calibrate the fluid-solid interaction in the models.

Introduction

A large number of technologies and natural phenomena involve liquids in nanometer-sized cavities. In all these situations, confinement confers the liquid unique properties, which are generally different from the bulk.[1,2] In particular, confined liquids often exhibit hysteresis, which points at the existence of metastable states.[3]

A typical hysteretic behavior is observed with vapor sorption in mesoporous solids, which exhibit adsorption/desorption hysteresis.[4] Questions about the nature of the adsorption and desorption branches, and the origin of hysteresis are almost as old as sorption experiments themselves.[5,6] The classical explanation builds on the different shape of the free surface of the adsorbed phase during adsorption and desorption.[7,8] In the textbook case of infinitely long cylindrical pores, adsorption occurs through the progressive thickening of a uniform liquid film covering the pore wall, while desorption occurs through the displacement of hemispherical menisci starting from the pores mouth inwards. As the curvature of the menisci is different in both cases - cylindrical or spherical - it follows from Kelvin's law that the two processes have to take place at different relative pressures.[4,9] A more general and modern understanding of these phenomena invokes the metastable or equilibrium nature of the adsorption and desorption branches of the isotherms.[10–12]

In addition to its scientific interest, the question of the nature of the adsorption and desorption branches has very practical consequences for experimental methods aiming at determining pore size distributions from sorption data. In that matter, the International Union of Pure and Applied Chemistry (IUPAC) supports the general view that adsorption is metastable and that desorption is an equilibrium process.[13] In the face of conflicting evidence

and of open questions in the field,[14–24] however, this should be understood as a temporary and mostly pragmatic recommendation.

When analyzing the thermodynamics of liquids in large mesopores, a classical approach consists in assuming three additive contributions to the free energy, namely: the macroscopic chemical potential difference between the vapor and liquid phases, the energy of the liquid free surface, and the van-der-Waals interactions between the liquid and the solid. Considering the specific case of a cylindrical pore with diameter D in contact with a vapor at temperature T and partial pressure P/P_0, the so-calculated free energy takes the following dimensionless form as a function of the radial position of the liquid-vapor interface r_I

$$\bar{\Omega} = 4 \ln \left[\frac{P}{P_0} \right] \left(\frac{r_I}{D} \right)^2 + 8 \frac{\lambda}{D} \left(\frac{r_I}{D} \right) + \frac{8}{D^2} \int_{D/2-r_I}^{D/2} \left(\frac{D}{2} - t \right) F(t) \, \mathrm{d}t \tag{1}$$

where the pore is empty for $r_I = D/2$, and it is saturated with liquid for $r_I = 0$. In this expression $\lambda = \gamma v_m/(k_B T)$ is a characteristic length of the liquid, where v_m is the molecular volume, γ is the surface tension of the liquid, and $F(t)$ is a dimensionless expression of the disjoining pressure in the adsorbed film resulting from van der Waals forces. The free energy in Eq. (1) is referred to as the Derjaguin-Broekhoff-de Boer approximation,[25,26] and it has been shown to be as accurate as Grand Canonical Monte Carlo (GCMC)[27] or non-local density functional theory (NLDFT)[11,28,29] for pore larger than about 5 nm.

To illustrate the question of metastable versus equilibrium states, Fig. 1a plots the three contributions to the free energy for a pore with diameter $D = 10$ nm, at four different vapor pressures, with parameters λ and $F(t)$ corresponding to nitrogen sorption on silica (see Supporting Information). The free energy is plotted against the radial position of the interface r_I, which is the only degree of freedom of the system in this geometrically ideal case. At any relative pressure $P/P_0 < 1$ the chemical potential contribution is minimal for $r_I = D/2$, because macroscopic thermodynamics opposes condensation below saturation. The surface energy is the lowest for $r_I = 0$ because this minimizes the surface area of the

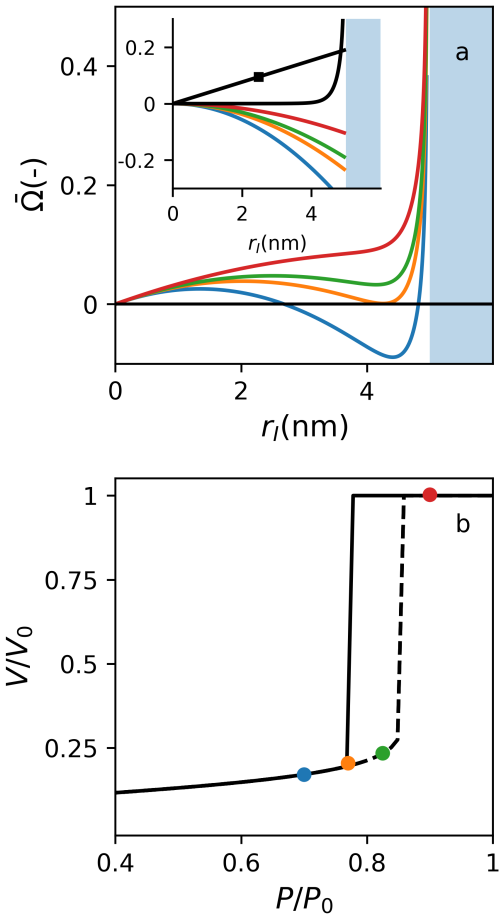

Figure 1: (a) Pressure-dependent free energy of an adsorbed liquid film in a cylindrical pore with diameter $D = 10$ nm as a function of the radial position r_I of the liquid free surface for $P/P_0 = 0.7$ (blue), 0.79 (orange), 0.82 (green) and 0.9 (red). The inset displays the three contributions to the free energy: the chemical potential difference between liquid and vapor (same color as in the main graph), van-der-Waals interaction with pore wall (black line), and energy of the liquid free surface (■). (b) Corresponding sorption isotherm, with metastable (dashed) and equilibrium (solid) branches, and with colored dots highlighting the pressures considered in a.

liquid-vapor interface. The van-der-Waals contribution is minimal also for $r_I = 0$, because filling the pore with condensate maximizes its interaction with the solid. Depending on the pressure, the resulting free energy may exhibit more than one local minimum, which results in the coexistence of equilibrium and metastable states. At low pressure, the global minimum of $\bar{\Omega}$ is for r_I slightly smaller than $D/2$, corresponding to a thin liquid film covering the solid (blue in Fig. 1). The filled pore configuration ($r_I = 0$) is then a metastable state. At intermediate pressure, the situation is reversed: the film configuration is metastable and the filled pore is the true equilibrium (green in Fig. 1). The particular pressure where the film configuration ceases to be a local minimum is referred to as the spinodal pressure. Beyond that point, the only local minimum left in $\bar{\Omega}$ is the saturated pore (red in Fig. 1).

Whether metastable or equilibrium states are observed in practice, depends on the possibilities that the system offers to overcome the free-energy barrier between the saturated-pore and thin-film configurations (Fig. 1). This generally depends on structural characteristics that are not captured by the cylindrical pore model.[17,19,22,30–34] When the film is the most stable configuration, *i.e.* at low pressure, the free-energy barrier is classically analyzed in terms of the pore constrictions that have to be crossed by receding menisci, starting from the pore mouths at the outer surface of the material.[35,36] The possibility of cavitation is also discussed in this context.[36–40] At high-pressure, when the film configuration is metastable, structural defects also play an important role. In that pressure range, local constrictions, pore corrugation, or smaller pores in a network may act as nucleation sites for capillary bridge formation, which can provide a low-energy pathway to reach the saturated state.[19,24,28,38,41] In disordered porous solids, the subsequent propagation of condensation regions depends critically on pore connectivity.[42] There is also increasing evidence that the mechanisms underlying capillary condensation and evaporation are temperature-dependent,[24,36,43,44] due notably to the possibility of activated condensation.[21,23] Finally, qualitatively different hysteresis are also observed for liquid or solid adsorbates.[15]

The status of adsorption/desorption experiments as a characterization technique adds to

the difficulty of investigating the metastable or equilibrium nature of capillary condensation and evaporation. How to validate or contradict any theory of sorption, if the pore sizes needed as an input to the theoretical calculations are partially inferred from sorption experiments themselves? The present paper focuses on a series of ordered mesoporous silicas of the type SBA-15,[45] the pore size of which can be reliably estimated independently of any sorption data through small-angle scattering.[46,47] Due to their ordered porous structure, SBA-15 materials exhibit strong scattering peaks in Small-Angle X-ray Scattering (SAXS) experiments, the relative intensities of which can be analyzed in terms of mesopore sizes.[48,49] We systematically analyze SAXS and sorption data measured on a series of SBA-15 materials. Based on the SAXS-derived pore sizes the equilibrium and spinodal pressures are calculated in the context of a DBdB model and compared to the experimental capillary condensation and evaporation pressures for nitrogen, argon, and water.

Materials and Methods

The SBA-15 ordered mesoporous materials were synthesized according to the classical three-step liquid-crystal templating procedure, namely:[45] (i) the preparation of an aqueous surfactant solution, (ii) the addition of the silica precursor and aging, (iii) the washing out of the surfactant and calcination. In situ scattering experiments show that spherical micelles are first formed, which transform to rod-like structures upon addition of the precursor.[50] The mesopores in the final materials are the negative replicas of the latter cylindrical micelles.

In practice, 16.2 g of surfactant (Pluronic123 by Sigma Aldrich) was added to 500 ml of deionized water and solubilized by adding a concentrated acidic solution. The solution was mixed for 24 hours at room temperature. From the so-obtained micelle suspension four batches of 115 ml were taken and put into four Teflon containers. The silica precursor was added to each container with a fixed molar ratio of 1/0.0165 for precursor and surfactant.[51] The containers were sealed and the solutions were vigorously stirred for 1 hour, and then

left unstirred for the rest of the 24 h at a given temperature T_1 to let the precursor undergo hydrolysis and condensation, followed by an additional 48 h at a higher temperature T_2 for hydrothermal treatment. At that stage, all reacting solutions had transformed into a gel, which was removed from the containers, washed by centrifuging twice with water and once with ethanol, and finally calcined in air at 550 °C for 6 h. This procedure typically produced of the order of 1 g of material per container.

The present paper is based on a total of fourteen SBA-15 materials (see Tab. SI-1). The complete dataset covers samples synthesized with either sulfuric or hydrochloric acid, at concentrations 0.8 M or 1.6 M, with either tetraethyl orthosilicate (TEOS), tetramethyl orthosilicate (TMOS) or tetrakis(2-hydroxyethyl)orthosilicate (EGMS) as silica precursor. The hydrolysis/condensation temperature T_1 ranges from 15 °C to 45 °C, with hydrothermal treatment at $T_2 = 100$ °C.

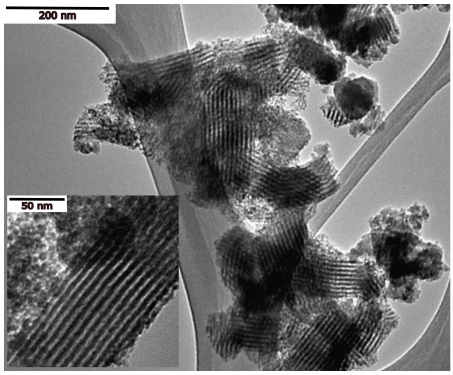

Figure 2: Transmission electron micrograph of a SBA-15 sample, displaying the large-scale grain structure and the parallel arrays of linear mesopores at smaller scale (inset).

The typical structure of SBA-15 materials is displayed in the transmission electron micrographs (TEM) of Fig. 2. The large-scale structure is that of porous grains a few hundreds of nanometers across, the inner structure of which consists in regularly stacked parallel mesopores. Because only projections of the structure are accessible through TEM, the technique is not suitable for quantitative characterization. Moreover, the sampling is extremely poor. The amount of material visible in the inset of Fig. 2 is of the order of a femtogram (10^{-15}g), which makes it difficult to ascertain whether electron micrographs are representative of the

macroscopic material. The typical sampling of small-angle scattering is on the milligram-scale, which is a twelve-orders-of-magnitude improvement compared to microscopy.[52]

Small-angle scattering of the SBA-15 materials was measured either on a Xenocs Xeuss laboratory instrument, with a molybdenum X-ray source with wavelength $\lambda = 0.7107$ Å, or at the Belgian beamline BM26 at the European Synchrotron Radiation Facility (ESRF, Grenoble) with $\lambda = 0.8856$ Å. In both cases silver behenate was used for angular calibration, and the isotropic intensities measured on two-dimensional detectors were converted to one-dimensional scattering patterns using the ConeX software.[53] In order to make the data independent of the specific wavelength used in the experiments, they are expressed as the scattered intensity against scattering wave vector q defined as

$$q = \frac{4\pi}{\lambda} \sin\left[\frac{\theta}{2}\right] \tag{2}$$

where θ is the scattering angle.

Nitrogen adsorption-desorption isotherms were measured at 77 K on a Micromeritics ASAP 2420MP volumetric device. Prior to analysis, the samples were outgassed under high vacuum for 5 hours at ambient temperature, followed by 5 hours at 270°C. Argon adsorption-desorption isotherms were collected at 87 K using a 3P Instruments Cryotune 87 device connected to one of the analysis ports of the gas adsorption instrument. Water adsorption-desorption isotherms were collected by Dynamic Vapor Sorption (DVS) with a DVS-Intrinsic (SurfaceMeasurementSystems) at 40 °C. The samples were first dried under a stream of dry nitrogen for 5 hours. Then, increasing steps of 10 % R.H. up to 90 % R.H. were applied, followed by a decrease down to 0 % R.H. At each step, the mass was recorded until a stabilization criterion of $dm/dt < 0.0015$ % was attained. The isotherms were constructed by plotting the equilibrated mass *vs.* the applied relative humidity.

The comprehensive nitrogen and argon sorption data discussed in the paper, as well as the corresponding small-angle scattering patterns can be downloaded from the authors'

institutional data repository.[54,55]

Results

Small-angle x-ray scattering

An example of the SAXS pattern measured on a SBA-15 sample is shown in Fig. 3. The data exhibit the scattering peaks typical of materials with P6mm symmetry,[48,49] which testifies to the overall structure of the material consisting of cylindrical pores positioned parallel to each other with hexagonal packing.

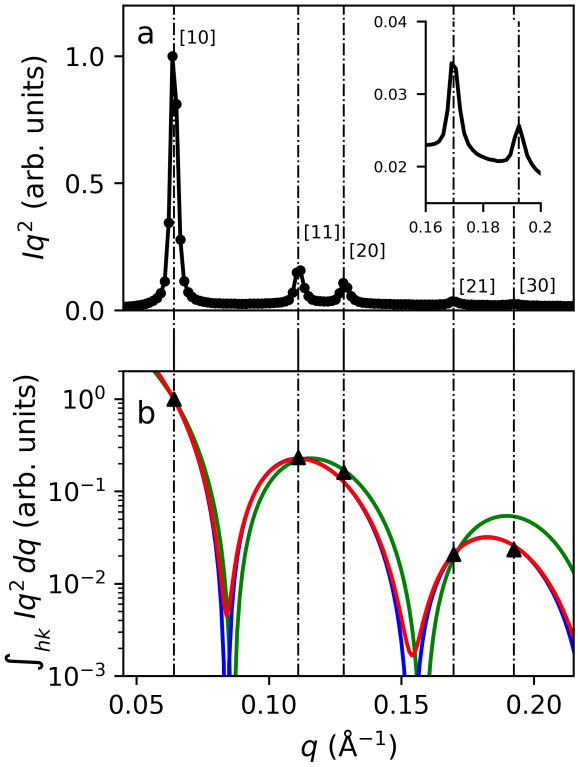

Figure 3: Example of SAXS intensity of a SBA-15 sample (a), together with the integrated intensities of all peaks (b). The inset in (a) highlights the peaks [2 1] and [3 0]. In (b) the symbols (▲) are the data and the solid lines are the form factors of monodispersed cylindrical pores (green), monodispersed cylindrical pores with Debye-Waller lattice disorder (blue), and polydispersed pores with Debye-Waller disorder (red).

The position of the peaks depends only on the spacing a between neighboring mesopores,

through

$$q_{hk} = \frac{4\pi}{a\sqrt{3}}\sqrt{h^2 + k^3 + hk} \tag{3}$$

where $[h\ k]$ are the Miller indices of the peaks, which are also recalled in Fig. 3. The dashed vertical lines in Fig. 3 were obtained by inferring the lattice parameter a from the position of the [0 1] peak, and calculating the higher orders through Eq. (3). The relevant value for the figure is $a = 113$ Å.

The structural information about the pore size is contained in the relative intensities of the peaks. The quantitative relation is the following[48,49,56]

$$\frac{1}{M(h,k)}\int_{hk} I(q)q^2 \mathrm{d}q = K\,|A(q_{hk})|^2 \tag{4}$$

where the integral on the left-hand side is the area under the $[h\ k]$ peak in Fig. 3a, with q^2 being a Lorentz factor accounting for the random orientation of the grains, and $M(h,k)$ is the multiplicity of the specific peak. In the case of Fig. 3, the multiplicity is 6 except for peak [2 1], for which it is 12. In the right-hand side, $A(q)$ is the Fourier transform of the electron-density profile within the hexagonal unit cell, and K is a normalization factor. The relation of the SAXS to the pore size is through the q-dependence of $A(q)$.

Three different geometrical models are considered in Fig. 3b, which are described in detail in Sec. SI-2. The data are normalized to the intensity of peak [0 1], which makes the constant K irrelevant for the analysis. The simplest model (Model 0) assumes monodispersed cylindrical pores positioned exactly on the nodes of a hexagonal lattice, with the pore diameter D as single fitting parameter (green in Fig. 3b). In the next model (Model 1), the pores are only statistically centred on the nodes of the lattice with Gaussian deviations (Debye-Waller disorder). In that case, the two fitting parameters are the diameter D and the standard deviation σ_a of the pore position (blue in Fig. 3b). Finally, in Model 2 the pores are additionally allowed to be polydispersed. This adds the standard deviation of the diameter distribution σ_D, as a third fitting parameter in addition to D and σ_a (red in Fig.

3b). The qualities of the fits expectedly improves when passing from one model to the next, as additional structural characteristics of the materials are accounted for (see Fig. SI-7). In the rest of the paper, the mesopore sizes are expressed as $D \pm \sigma_D$ with the values obtained from the fitting of Model 2. In the case of Fig. 3, the pore diameter is 9.1 ± 0.2 nm and the randomness in pores position is $\sigma_a \simeq 1.3$ nm. The pore sizes estimated from the other models differ from Model 2 by less than 0.5 nm (see Fig. SI-8).

A popular approach to analyze the scattering of SBA-15 assumes a progressive transition from the mesopore to the silica wall, with a linear density profile in between (see Model 3 in Sec. SI-2). This model was historically interpreted in terms of a hypothetical microporous corona surrounding the mesopore,[32,48] but the same scattering can be understood in terms of nanometer-scale corrugation of the mesopores, which was later confirmed by direct electron tomography reconstruction.[57–59] In that respect, it has to be stressed that the SAXS peak intensities cannot discriminate pore size variablity between mesopores, from the variability along the mesopores.[58] Therefore Model 2 is best interpreted in terms of corrugated mesopores, where the longitudinal variability of the pore section results from the fluctuations of both their diameter and position through parameters σ_D and σ_a.

Sorption results

The argon and nitrogen sorption isotherms measured on the same material as in Fig. 3 are plotted in Fig. 4. The insets of the figure display the corresponding t-plots, whereby the experimental adsorption data are plotted against the statistical thickness $t(P/P_0)$ of the adsorbed film on a reference non-porous silica at the same pressure.[4,60,61] The specific reference we use throughout this work is LiChrospher SI-1000, both for nitrogen[62] and argon[63] adsorption. The t-plots in Fig. 4 exhibit two linear trends (dashed lines), from the slopes and intercepts of which, we extracted the micro- and meso-pore contributions to the total pore volume V_μ and V_m, as well as the contributions to the surface area from the mesopores A_m and from the external surface of the grains A_{ext}.

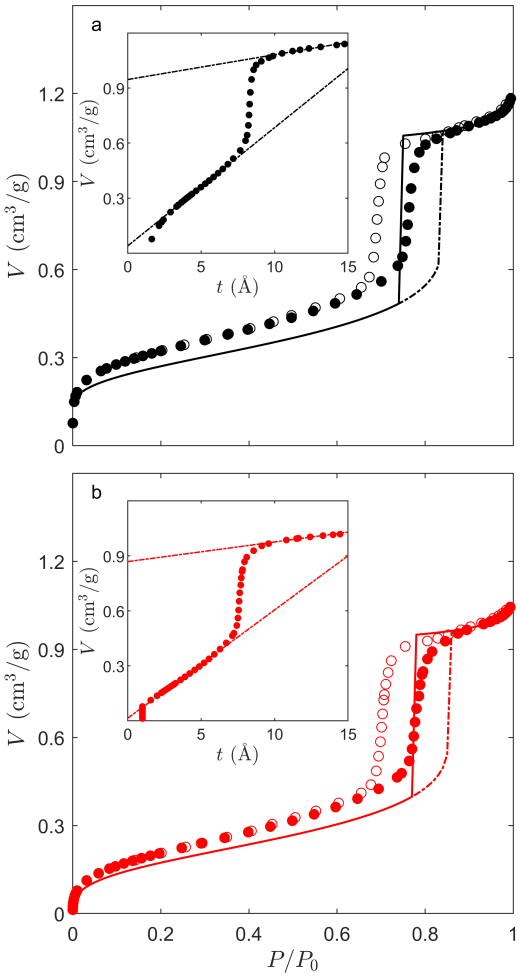

Figure 4: Example of nitrogen (a) and argon (b) sorption data on one of the SBA-15 samples and its analysis. The full and empty symbols are the experimental adsorption and desorption branches. The dashed and solid lines are the calculated metastable and equilibrium states, based on a DBdB calculation with the pore size estimated from SAXS. The insets display the corresponding t-plots.

The lines added to the main graphs in Fig. 4 are calculated from the Derjaguin-Broekhoff-de Boer (DBdB) analysis assuming the mesopore size D obtained from SAXS, for both the metastable (dashed line) and the equilibrium (solid line) states. As the DBdB accounts neither for the micropores nor for the external surface area, the calculations are plotted as

$$V = V_\mu + A_{ext} \times t\,(P/P_0) + V_m \times V_{DBdB}\,(P/P_0, D) \tag{5}$$

where $t(P/P_0)$ is the thickness adsorbed on a flat surface, and V_μ, A_{ext} and V_m are taken from the t-plot. The physical parameters that enter the DBdB calculations are the classically accepted values $\gamma = 8.85$ mJ/m^2 and $v = 34.6$ cm^3/mol for the surface tension and molar volume of liquid nitrogen at 77 K,[4] and $\gamma = 11$ mJ/m^2 and $v = 28.53$ cm^3/mol for liquid argon at 87 K.[63,64] In addition, the disjoining pressure term $F(t)$ in Eq. (1) was obtained by calibrating the BdB model on the same non-porous reference as assumed in the t-plots.[19,29,65] In other words, we assumed

$$F(t) = \ln\left[\frac{P}{P_0}\right] \tag{6}$$

where t is the thickness of argon or nitrogen film adsorbed on LiChrospher Si-1000 at pressure P/P_0. The details of the procedure are reported in Sec. SI-3.

A striking observation in Fig. 4, is that the calculated equilibrium isotherm does not coincide with the desorption branch, neither for argon nor for nitrogen sorption. Instead, the calculated equilibrium transition seems to describe best the capillary condensation. The situation is not specific to one particular SBA-15 sample. Figure 5 compares systematically the experimental condensation and evaporation pressures to the spinodal and equilibrium transition pressures calculated from the DBdB model based on the actual pore sizes evaluated by SAXS. The error bars on the pressures are the width of the transitions in the adsorption and desorption isotherms, and the errors on the size is the standard deviation of the diameter σ_D based on the polydispersed model. On that graph, the spinodal does not seem to correspond to any experimental transition pressures. In the case of argon and

nitrogen (Figs. 5a and 5b), the experimental condensation pressures almost coincide with the calculated equilibrium transition.

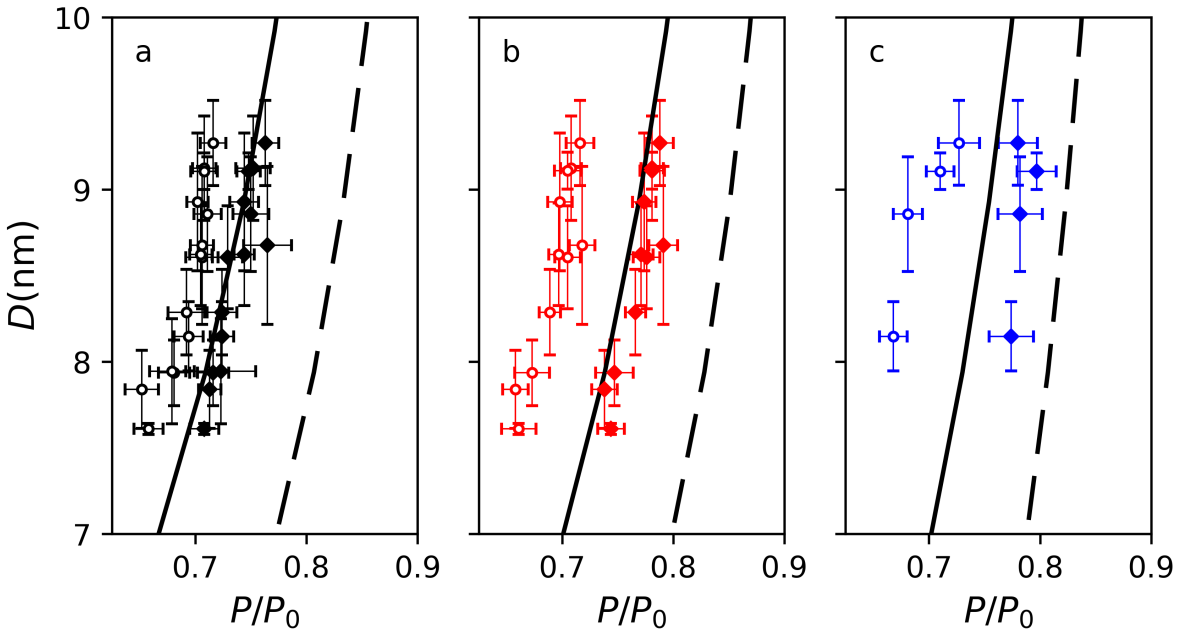

Figure 5: Capillary condensation and evaporation pressures (full and empty symbols, respectively) obtained experimentally from nitrogen (a), argon (b), and water (c) sorption experiments, plotted against the mesopore sizes from SAXS. The lines show the equilibrium (solid) and spinodal (dashed) transition pressures calculated by DBdB approach.

Figure 5c extends the analysis to the case of capillary condensation and evaporation of water in some of the same SBA-15 materials. Unlike nitrogen and argon, water does not perfectly wet silica, which makes its adsorption analysis more complex than the DBdB scenario. This is further complicated by the fact that the contact angle depends on the relative humidity[66] and that the very structure of SBA-15 is not stable in contact with water.[67] Not unexpectedly, the spinodal and equilibrium transition pressures calculated while ignoring these difficulties, do not coincide with the experimental capillary condensation or evaporation of water.

Discussion

The main result of the paper is that capillary condensation in all the considered SBA-15 materials occurs close to thermodynamic equilibrium, both for nitrogen and for argon adsorption. Our discussion of this fact focuses on three main points, namely: the accuracy of the pore size determination through SAXS, which is central to our argument; considerations on the possible origin of the discrepancy with other works supporting the spinodal-condensation view; and practical consequences for porous materials characterization by sorption methods.

The determination of mesopore diameters from small-angle scattering in ordered materials follows a classical and well-established procedure.[48,49,57,68–70] To build confidence on them, we here compare them with independent estimations based on pore volumes and/or areas. The latter are obtained from sorption data, but they do not rely on any assumption concerning the nature of the adsorption and desorption branches. A classical, area-based, approach for cylindrical pores consists in estimating the mesopore size as a volume-to-area ratio,[71] namely

$$D_A = \frac{4V_m}{A_m} \tag{7}$$

where the volume and area V_m and A_m are those of the mesopores, estimated from the t-plots. The so-calculated D_A's are reported in Fig. 6 against the SAXS-derived values D. Expectedly the values of D_A underestimate the actual pore size D, because volume-to-area ratios are controlled by the smallest structures. The micropores within the pore wall do not contribute to the mesopore surface area A_m, but the latter is still very much affected by surface corrugation.[57,58] Based on the detailed structural analysis of electron tomography and small-angle scattering data, one estimates that corrugation increases the surface area of SBA-15 by as much as 60% compared to a smooth cylindrical pore with identical average diameter (See appendix B of Ref. 19). This order of magnitude is the same as the mismatch in Fig. 6, which further confirms the corrugation of the considered SBA-15 materials.

An alternative estimation of the mesopore size in SBA-15 consists in comparing the

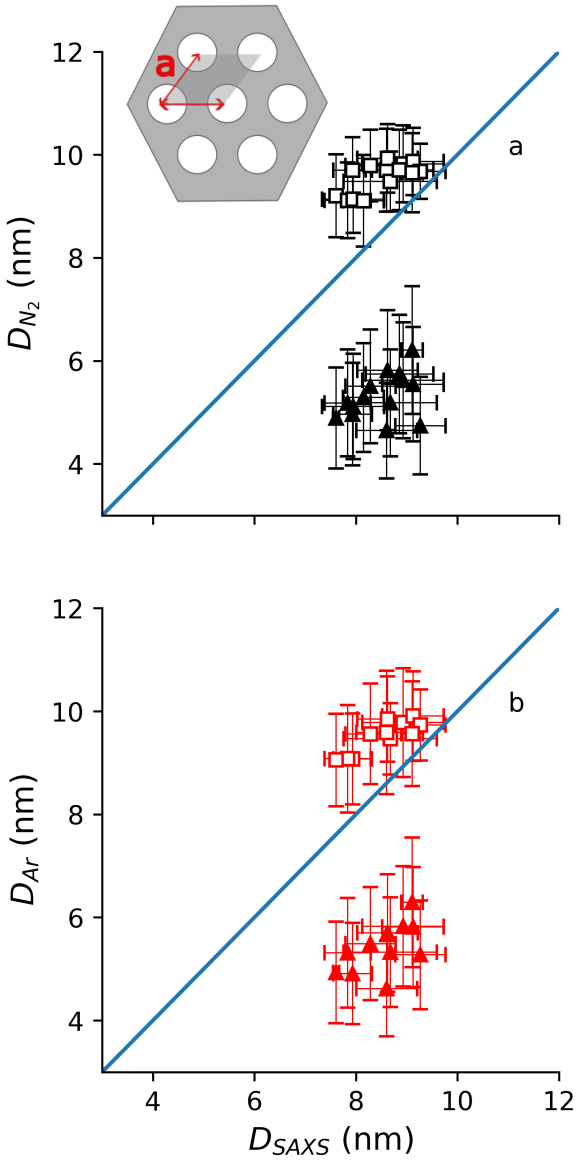

Figure 6: Comparison of SAXS-derived mesopore sizes D_{SAXS}, with geometrical estimates based on the areas and volume inferred from sorption data through Eq. (7) shown as (▲), and through Eq. (9) shown as (□). Figures a and b result from nitrogen and argon sorption, respectively. The inset is a sketch of the material's unit cell.

mesopore volume to the volume of the unit cell (see inset of Fig. 6a). This yields the following expression for the mesopore volume fraction

$$\phi_m = \frac{(\pi/4)(D^2 + \sigma_D^2)}{(\sqrt{3}/2)a^2} \tag{8}$$

In this equation, the numerator is the average area of the mesopore section (accounting for polydispersity) and the denominator is the area of the unit cell where a is the lattice parameter (see inset of Fig. 6). On the other hand, the mesopore volume fraction can be estimated from adsorption volumes as $\phi_m = V_m/(V_m + V_\mu + 1/\rho_s)$ where $\rho_s \simeq 2.2$ g/cm^3 is the skeletal density of silica. This eventually leads to the following estimate of the mesopore diameter[72]

$$D^2 + \sigma_D^2 = \frac{2\sqrt{3}}{\pi} \frac{\rho_s V_m}{1 + \rho_s(V_m + V_\mu)} \times a^2 \tag{9}$$

We hereafter call D_V the pore diameter obtained by setting $\sigma_D = 0$ in this equation, because it is a volume-based estimate of the pore size. The values of D_V are found to slightly overestimate D (see Fig. 6), which was indeed expected because they were obtained by setting $\sigma_D = 0$ in Eq. (9). It has to be stressed that the polydispersity from the SAXS cannot discriminate a collection of perfectly cylindrical pores with statistically distributed diameters from the case of corrugated pores with a circular cross section, *i.e.* with statistical distribution of the diameters along the pore length.[57,58] Therefore, mesopore corrugation can also explain the overestimation resulting from Eq. (9).

Globally, two conclusions are drawn from Fig. 6. First, the mesopore sizes derived from the SAXS are accurate, and they are intermediate between the independently estimated lower and upper bounds D_A and D_V as they should. Second, the systematic differences between D_A, D_V and D all point at significant deviations from geometrically ideal cylindrical pores, *i.e.* at pore corrugation.

Several graphs similar to Fig. 5 are found in the literature, based on a variety of ordered mesoporous materials, some of which seem to support the spinodal condensation hypoth-

esis,[28,73] others not.[72,74] When analyzing them, it is not easy to track down how the pore sizes were determined exactly, because they put together characterization works conducted by different authors. Moreover, the size estimations occasionally rest on simplified geometrical assumptions that do not apply to SBA-15, as we now understand better than when some of these works were conducted.[32,48,57,75] As an example, consider the data underlying Fig. 3 of Ref. 73 (reproduced from Fig. 9 of Ref. 28), which is cited by the IUPAC technical report to support both equilibrium desorption and metastable adsorption.[13] Many data points in that figure rest on pore sizes determined through a volume-to-area ratio similar to Eq. (7),[72,76,77] and are therefore expected to significantly underestimate the pore sizes. Some data points in the same figure result from applying a method similar to Eq. (9), but neglect both microporosity and mesopore polydispersity.[72,78] One of the references used in the figure acknowledges discrepancies between the values of D_V and D_A and attempts to reconcile them with non-standard values for the area occupied by an adsorbed nitrogen molecule.[77] Another reference considers a variety of pore size determinations on the same footing, and it is unclear which one of those was eventually used in the figure.[72] Yet a few other references use adsorption/desorption measurements themselves to to determine the pore sizes, using NLDFT[79,80] or even BJH.[45,81] Because these specific data points do not seem to be based on any independent determination of the pore size, they cannot reasonably be used as arguments in favor or against any physical theory of capillary condensation. None of these issues apply to the data presented in Fig. 5, for which all the pore sizes have been determined independently and systematically through SAXS.

A significant difficulty when discussing the metastable or equilibrium nature of capillary condensation and evaporation, is that the question can only be addressed in the context of models, and models have to be calibrated. Model parameters describing fluid-fluid interactions are not problematic; for DBdB they are captured by the surface tension and the molecular volume. By contrast, calibrating the fluid-solid interaction requires one to chose a reference non-porous solid, and to adjust the relevant parameters to match experimental

multilayer adsorption data on that solid. In the case of DBdB, this is the role of the standard isotherm in Eq. (6). Because truly non-porous solids have vanishingly small surface areas, all standard isotherms available in the literature have been measured on surfaces that are not strictly flat. Any deviation from a flat surface geometry results in increased adsorption, usually through inter-particle capillary condensation.[4,9,62] Building a thermodynamic analysis on such a biased reference isotherm would overestimate the fluid-solid interactions, and it would shift the calculated mesopore filling or emptying transitions (both equilibrium and spinodal) towards lower relative pressures. The situation is qualitatively similar for physically more sophisticated models such as NLDFT, where fluid-solid interaction parameters have also to be calibrated on reference adsorption data.[73,79]

The reference used throughout this paper for nitrogen and argon adsorption is LiChrospher - a large-grain precipitated silica - which is widely considered to provide extremely accurate standard isotherms.[62,63] In particular, it was proven to be more suitable than other references for explicitly analyzing inter-particle condensation.[82] It was also identified as the preferred high-pressure reference when building composite reference isotherms.[61,83] For the sake of completeness a variety of published standard isotherms are compared in Fig. SI-9, in some of which parasitic capillary condensation is manifest. The impact this has on the calculated transition pressures (spinodal and equilibrium) is illustrated in Figs. SI-10 to SI-12 for nitrogen, argon and water.

The findings in Fig. 5 have very practical consequences when it comes to analyzing sorption data in terms of pore size distributions. To illustrate this point, Fig. 7 compares the actual mesopore sizes of the SBA-15 samples to the sizes that would be inferred from the sorption data based on various assumptions: delayed (metastable) capillary condensation (Fig. 7a), equilibrium capillary evaporation (Fig. 7b), and equilibrium capillary condensation (Fig. 7c). The first two assumptions underestimate systematically the mesopore size by more than 20 %. Only the last assumption leads to an unbiased estimate of the mesopore size. It is a striking twist that the best results are here obtained with what might be called

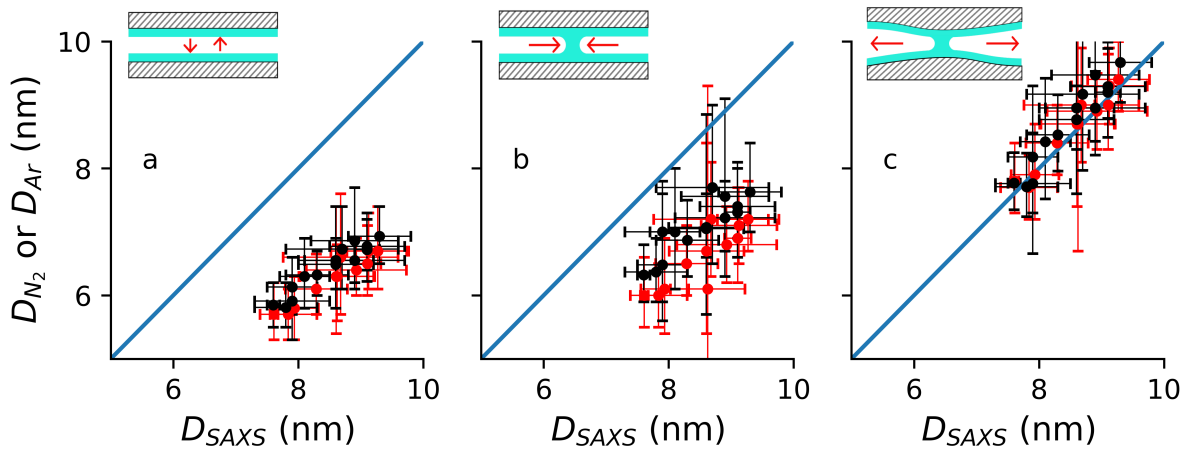

Figure 7: Comparison between pore sizes estimated from SAXS and from sorption data analysis with different assumptions: (a) metastable adsorption,(b) equilibrium desorption, and (c) equilibrium adsorption.The black and the red markers result for nitrogen and argon sorption, respectively. The horizontal error bars are the polydispersity from SAXS σ_D, and the vertical error bars are the width of the size distribution inferred from sorption analysis.

the "wrong model", *i.e.* by applying to the adsorption isotherm a data-analysis procedure that one would traditionally advocate for the desorption isotherm.[4,13,71]

The observation of equilibrium capillary condensation in SBA-15 strongly hints at the presence of spherical menisci during adsorption. Such menisci are traditionally discussed in the context of desorption - where they are expected to form at the pore mouth close to saturation and recede inwards - but they could also result from capillary bridges. Capillary bridges have long been discussed as intermediate steps in the process of capillary condensation, either as a result of capillary-like instability in perfectly cylindrical pores,[24,38,84] or on geometrical defects such as corrugation or local constrictions.[19,31,34,85,86] In both cases they reduce the free-energy barrier below the values relevant to Fig. 1. In the event that capillary bridges would be created during adsorption, capillary condensation would proceed through their thickening at a pressure lower than the spinodal (inset of Fig. 7c). Such a scenario would also provide a simple explanation for the otherwise puzzling observation that the capillary condensation pressure in a single pore appears not to depend on whether its ends are open or closed.[14,15,80] In the specific case of SBA-15 corrugated mesopores,[57,59]

modelling work based on independent SAXS and microscopy data suggests that capillary bridges are indeed expected to form on geometrical defects.[19] It remains, however, to be ascertained whether geometrical defects alone can explain the experimental results reported in the present paper.

Conclusion

A Derjaguin-Broekhoff-de Boer analysis of argon and nitrogen sorption in SBA-15 ordered mesoporous silica - building on independently-measured pore sizes through small-angle scattering - shows that capillary condensation occurs close to thermodynamic equilibrium in these materials. This result adds to a growing list of experimental and theoretical arguments against the historical and still popular conception that adsorption is a metastable process, and that capillary condensation is a spinodal transition.

A critical analysis of published results, suggests that earlier studies might have been biased towards underestimating the actual equilibrium and spinodal pressures in SBA-15 materials. Small-angle scattering indeed shows that calculations based on volume-to-area ratios lead to a severe underestimation of the mesopore sizes, by as much as 2 nm, even when micropores are excluded. In addition, the choice of a specific standard isotherm to calibrate the fluid-solid interaction proves critical. Because adsorption on truly flat surfaces is difficult to measure, most published reference isotherms are biased upwards by inter-particle condensation effects, which eventually adds to the underestimation of the equilibrium and spinodal pressures.

It has finally to be stressed that in spite of pore corrugation SBA-15 is generally considered to be an ordered material. And structural disorder is widely acknowledged to destabilize metastable adsorption states, if only by providing nucleation sites for capillary condensation. Our findings are therefore likely to concern a wide range non-ordered materials as well. When working with mesoporous materials in general, we submit that it might be fruitful to consider

that capillary condensation is an equilibrium, not a metastable, transition.

Acknowledgement

CJG is grateful to the Funds for Scientific Research (F.R.S.-FNRS, Belgium) for a research associate position, and for supporting this work through grant PDR T.0100.22. AFL thanks the University of Liège (Fonds Spéciaux pour la Recherche FSR) and the Fonds de Bay for their financial supports. AB thanks the University of Liège, the FEDER Funds and the FMF (Films Multi-Fonctionnels) portofilio for supporting this work through the BIODEC project. All authors are grateful to Mrs. Kristien Van der Flaas (KULeuven) and to Dr. Martin Rosenthal (European Synchrotron Radiation Facility, DUBBLE-BM26) for their assistance with the SAXS measurements.

Supporting Information Available

Comprehensive characterization data of all samples, and details about data analysis procedures. All data are available for downloading from the authors' institutional data repository (10.58119/ULG/L8PJJK and 10.58119/ULG/S0HYHL). This material is available free of charge via the Internet at `http://pubs.acs.org/`.

References

(1) Coasne, B.; Galarneau, A.; Pellenq, R. J. M.; Di Renzo, F. Adsorption, intrusion and freezing in porous silica: the view from the nanoscale. *Chem. Soc. Rev.* **2013**, *42*, 4141.

(2) Kavokine, N.; Netz, R. R.; Bocquet, L. Fluids at the nanoscale: from continuum to subcontinuum transport. *Ann. Rev. Fluid Mech.* **2021**, *53*, 377– 410.

(3) Debenedetti, P. *Metastable Liquids: Concepts and Principles*; Princeton University Press: Princeton, 1996.

(4) Gregg, S. J.; Sing, K. S. W. *Adsorption, Surface Area and Porosity*; Academic Press: London, 1982.

(5) Zsigmondy, R. Über die Struktur des Gels der Kieselsäure. Theorie der Entwässerung. *Zeitschrift für anorganische Chemie* **1911**, *71*, 356–377.

(6) Foster, A. G. The sorption of condensible vapours by porous solids. Part I. The applicability of the capillary theory. *Trans. Faraday Soc.* **1932**, *28*, 645–657.

(7) Cohan, L. H. Sorption hysteresis and the vapor pressure of concave surfaces. *J. Am. Chem. Soc.* **1938**, *60*, 433 to 435.

(8) Coelingh, M. B. Optische Untersuchungen über das Flüssigkeit-Dampfgleichgewicht in kapillaren Systemen. *Kolloid-Zeitschrift* **1939**, *87*, 251–272.

(9) Adamson, A. W.; Gast, A. P. *Physical Chemistry of Surfaces*; Wiley: New York, 1997.

(10) Neimark, A.; Ravikovitch, P.; Vishnyakov, A. Adsorption hysteresis in nanopores. *Phys. Rev. E* **2000**, *62*, R1493–R1496.

(11) Monson, P. Understanding adsorption/desorption hysteresis for fluids in mesoporous materials using simple molecular models and classical density functional theory. *Microp. Mesop. Mater.* **2012**, *160*, 47–66.

(12) Thommes, M.; Schlumberger, C. Characterization of nanoporous materials. *Ann. Rev. Chem. Biomol. Eng.* **2021**, *12*, 137–162.

(13) Thommes, M.; Kaneko, K.; Neimark, A. V.; Olivier, J. P.; Rodriguez-Reinoso, F.; Rouquerol, J.; Sing, K. S. Physisorption of gases, with special reference to the evaluation of surface area and pore size distribution (IUPAC Technical Report). *Pure Appl. Chem.* **2015**, *87*, 1051–1069.

(14) Coasne, B.; Grosman, A.; Ortega, C.; Simon, M. Adsorption in noninterconnected pores open at one or at both ends: A reconsideration of the origin of the hysteresis phenomenon. *Phys. Rev. Lett.* **2002**, *88*, 256102.

(15) Wallacher, D.; Künzner, N.; Kovalev, D.; Knorr, N.; Knorr, K. Capillary condensation in linear mesopores of different shape. *Phys. Rev. Lett.* **2004**, *92*, 195704, 1–4.

(16) Grosman, A.; Ortega, C. Nature of capillary condensation and evaporation processes in ordered porous materials. *Langmuir* **2005**, *21*, 10515 to 10521.

(17) Naumov, S.; Khokhlov, A.; Valiullin, R.; Kärger, J.; Monson, P. A. Understanding capillary condensation and hysteresis in porous silicon: Network effects within independent pores. *Phys. Rev. E* **2008**, *78*, 060601.

(18) Kleitz, F.; Bérubé, F.; Guillet-Nicolas, R.; Yang, C.-M.; Thommes, M. Probing adsorption, pore condensation, and hysteresis behavior of pure fluids in three-dimensional cubic mesoporous KIT-6 silica. *J. Phys. Chem. C* **2010**, *114*, 9344–9355.

(19) Gommes, C. J. Adsorption, capillary bridge formation, and cavitation in SBA-15 corrugated mesopores: A Derjaguin-Broekhoff-de Boer analysis. *Langmuir* **2012**, *28*, 5101–5115.

(20) Morishige, K. Nature of adsorption hysteresis in cylindrical pores: Effect of pore corrugation. *J. Phys. Chem. C* **2016**, *120*, 22508–22514.

(21) Hiratsuka, T.; Tanaka, H.; Miyahara, M. T. Comprehensive Modeling of Capillary Condensation in Open-Ended Nanopores: Equilibrium, Metastability, and Spinodal. *J. Phys. Chem. C* **2017**, *121*, 2687726886.

(22) Gommes, C. J.; Roberts, A. P. Stochastic analysis of capillary condensation in disordered mesopores. *Phys. Chem. Chem. Phys.* **2018**, *20*, 13646–13659.

(23) Bonnet, F.; Melich, M.; Puech, L.; Angls dAuriac, J.-C.; Wolf, P.-E. On Condensation and Evaporation Mechanisms in Disordered Porous Materials. *Langmuir* **2019**, *35*, 51405150.

(24) Morishige, K. Revisiting the nature of adsorption and desorption branches: Temperature dependence of adsorption hysteresis in ordered mesoporous silica. *ACS Omega* **2021**, *6*, 15964 –15974.

(25) Broekhoff, J.; de Boer, J. Studies on pore systems in catalysts: XII. Pore distributions from the desorption branch of a nitrogen sorption isotherm in the case of cylindrical pores A. An analysis of the capillary evaporation process. *J. Catal.* **1968**, *10*, 368–376.

(26) Derjaguin, B.; Churaev, N. Polymolecular adsorption and capillary condensation in narrow slit pores. *J. Coll. Interf. Sci.* **1976**, *54*, 157–175.

(27) Celestini, F. Capillary condensation within nanopores of various geometries. *Phys. Lett. A* **1997**, *228*, 84 – 90.

(28) Neimark, A. V.; Ravikovitch, P. I.; Vishnyakov, A. Bridging scales from molecular simulations to classical thermodynamics: Density functional theory of capillary condensation in nanopores. *J. Phys. Cond. Matter* **2003**, *15*, 347 – 365.

(29) Ustinov, E.; Do, D.; Jaroniec, M. Equilibrium adsorption in cylindrical mesopores: A modified Broekhoff and de Boer theory versus density functional theory. *J. Phys. Chem. B* **2005**, *109*, 1947 to 1958.

(30) Maddox, M.; Olivier, J.; Gubbins, K. Characterization of MCM-41 using molecular simulation: Heterogeneity effects. *Langmuir* **1997**, *13*, 1737–1745.

(31) Coasne, B.; Hung, F. R.; Pellenq, R. J. M.; Siperstein, F. R.; Gubbins, K. E. Adsorption of sample gases in MCM-41 materials: The role of surface roughness. *Langmuir* **2006**, *22*, 194–202.

(32) Ravikovitch, P. I.; Neimark, A. V. Density functional theory model of adsorption on amorphous and microporous silica materials. *Langmuir* **2006**, *22*, 11171–11179.

(33) Schneider, D.; Valiullin, R. Capillary condensation and evaporation in irregular channels: Sorption isotherm for serially connected pore model. *J. Phys. Chem. C* **2019**, *123*, 16239–16249.

(34) Enninful, H. R. N. B.; Schneider, D.; Enke, D.; Valiullin, R. Impact of geometrical disorder on phase equilibria of fluids and solids confined in mesoporous materials. *Langmuir* **2021**, *37*, 3521–3537.

(35) Thommes, M.; Smarsly, B.; Groenewolt, M.; Ravikovitch, P. I.; Neimark, A. V. Adsorption hysteresis of nitrogen and argon in pore networks and characterization of novel micro- and mesoporous silicas. *Langmuir* **2006**, *22*, 756–764.

(36) Bossert, M.; Grosman, A.; Trimaille, I.; Souris, F.; Doebele, V.; Benoit-Gonin, A.; Cagnon, L.; Spathis, P.; Wolf, P.-E.; Rolley, E. Evaporation process in porous silicon: Cavitation vs pore blocking. *Langmuir* **2021**, *37*, 14419–14428.

(37) Morishige, K.; Tateishi, N. Adsorption hysteresis in ink-bottle pore. *J. Chem. Phys.* **2003**, *119*, 2301 – 2306.

(38) Vishnyakov, A.; Neimark, A. V. Nucleation of liquid bridges and bubbles in nanoscale capillaries. *J. Chem. Phys.* **2003**, *119*, 9755 to 9764.

(39) Fan, C.; Do, D. D.; Nicholson, D. On the cavitation and pore blocking in slit-shaped ink-bottle pores. *Langmuir* **2011**, *27*, 3511–3526.

(40) Puibasset, J. Cavitation in heterogeneous nanopores: The chemical ink-bottle. *AIP Advances* **2021**, *11*.

(41) Röcken, P.; Somoza, A.; Tarazona, P.; Findenegg, G. Two-stage capillary condensation

in pores with structured walls: A nonlocal density functional study. *J. Chem. Phy.* **1998**, *108*, 8689 to 8697.

(42) Kikkinides, E. S.; Enke, D.; Valiullin, R. Gas Sorption Characterization of Porous Materials Employing a Statistical Theory for Bethe Lattices. *J. Phys. Chem. A* **2024**, *128*, 45734587.

(43) Morishige, K.; Tateishi, M. Accurate relations between pore size and the pressure of capillary condensation and the evaporation of nitrogen in cylindrical pores. *Langmuir* **2006**, *22*, 4165–4169.

(44) Qiu, X.; Yang, H.; Dejam, M.; Tan, S. P.; Adidharma, H. Experiments on the capillary condensation/evaporation hysteresis of pure fluids and binary mixtures in cylindrical nanopores. *J. Phys. Chem. C* **2021**, *125*, 5802–5815.

(45) Zhao, D.; Feng, J.; Huo, Q.; Melosh, N.; Fredrickson, G. H.; Chmelka, B. F.; Stucky, G. D. Triblock copolymer syntheses of mesoporous silica with periodic 50 to 300 angstrom pores. *Science* **1998**, *279*, 548–552.

(46) Glatter, O. *Scattering Methods and their Application in Colloid and Interface Science*.

(47) Gommes, C. J.; Jaksch, S.; Frielinghaus, H. Small-angle scattering for beginners. *J. Appl. Crystallogr.* **2021**, *54*, 1832–1843.

(48) Imperor-Clerc, M.; Davidson, P.; Davidson, A. Existence of a microporous corona around the mesopores of silica-based SBA-15 materials templated by triblock copolymers. *J. Am. Chem. Soc.* **2000**, *122*, 11925–11933.

(49) Förster, S.; Timmann, A.; Konrad, M.; Schellbach, C.; Meyer, A.; Funari, S. S.; Mulvaney, P.; Knott, R. Scattering curves of ordered mesoscopic materials. *J. Phys. Chem. B* **2005**, *109*, 1347–1360.

(50) Manet, S.; Schmitt, J.; Impror-Clerc, M.; Zholobenko, V.; Durand, D.; Oliveira, C. L. P.; Pedersen, J. S.; Gervais, C.; Baccile, N.; Babonneau, F.; Grillo, I.; Meneau, F.; Rochas, C. Kinetics of the formation of 2D-hexagonal silica nanostructured materials by nonionic block copolymer templating in solution. *J. Phys. Chem. B* **2011**, *115*, 11330 – 11344.

(51) Cao, L.; Man, T.; Kruk, M. Synthesis of ultra-large-pore SBA-15 silica with two-dimensional hexagonal structure using triisopropylbenzene as micelle expander. *Chem. Mater.* **2009**, *21*, 1144–1153.

(52) Gommes, C. J.; Prieto, G.; Zecevic, J.; Vanhalle, M.; Goderis, B.; de Jong, K. P.; de Jongh, P. E. Mesoscale Characterization of Nanoparticles Distribution Using X-ray Scattering. *Angew. Chem. Intl. Ed.* **2015**, *54*, 11804 11808.

(53) Gommes, C. J.; Goderis, B. *CONEX*, a program for angular calibration and averaging of two-dimensional powder scattering patterns. *Journal of Applied Crystallography* **2010**, *43*, 352–355.

(54) Belet, A.; Léonard, A.; Heinrichs, B. Small-angle scattering and sorption data in SBA-15 materials. 2024; `https://doi.org/10.58119/ULG/L8PJJK`, Accessed: 2024-07-05.

(55) Haidar, A.; Léonard, A.; Gommes, C. J. Small-angle scattering and sorption data in mesoporous materials. 2024; `https://doi.org/10.58119/ULG/S0HYHL`, Accessed: 2024-07-05.

(56) Gommes, C. J.; Prieto, G.; de Jongh, P. E. Small-angle scattering analysis of empty or loaded hierarchical porous materials. *J. Phys. Chem. C* **2016**, *120*, 1488–1506.

(57) Gommes, C. J.; Friedrich, H.; Wolters, M.; de Jongh, P. E.; de Jong, K. P. Quantitative characterization of pore corrugation in ordered mesoporous materials using image analysis of electron tomograms. *Chem. Mater.* **2009**, *21*, 1311–1317.

(58) Gommes, C. J.; Friedrich, H.; de Jongh, P. E.; de Jong, K. P. 2-Point correlation function of nanostructured materials via the grey-tone correlation function of electron tomograms: A three-dimensional structural analysis of ordered mesoporous silica. *Acta Mater.* **2010**, *58*, 770 – 780.

(59) Yuan, P.; Tan, L.; Pan, D.; Guo, Y.; Zhou, L.; Yang, J.; Zou, J.; Yu, C. A systematic study of long-range ordered 3D-SBA-15 materials by electron tomography. *New J. Chem.* **2011**, *35*, 2456.

(60) Lippens, B.; de Boer, J. Studies on pore systems in catalysts. V. The t-method. *J. Catal.* **1965**, *4*, 319–323.

(61) Galarneau, A.; Villemot, F.; Rodriguez, J.; Fajula, F.; Coasne, B. Validity of the t-plot method to assess microporosity in hierarchical micro/mesoporous materials. *Langmuir* **2014**, *30*, 13266–13274.

(62) Jaroniec, M.; Kruk, M.; Olivier, J. P. Standard nitrogen adsorption data for characterization of nanoporous silicas. *Langmuir* **1999**, *15*, 5410–5413.

(63) Kruk, M.; Jaroniec, M. Accurate method for calculating mesopore size distributions from argon adsorption data at 87 K developed using model MCM-41 materials. *Chem. Mater.* **2000**, *12*, 222–230.

(64) Vargaftik, N. B. *Tables on the thermophysical properties of liquids and gases*; Taylor & Francis, 1975.

(65) Broekhoff, J.; de Boer, J. Studies on pore systems in catalysts. IX. Calculation of pore distributions from the adsorption branch of nitrogen sorption isotherms in the case of open cylindrical pores A. Fundamental equations. *J. Catal.* **1967**, *9*, 8–14.

(66) Zandavi, S. H.; Ward, C. A. Nucleation and growth of condensate in nanoporous materials. *Phys. Chem. Chem. Phys.* **2015**, *17*, 9828–9834.

(67) Erko, M.; Wallacher, D.; Findenegg, G.; Paris, O. Repeated sorption of water in SBA-15 investigated by means of in situ small-angle x-ray scattering. *J. Phys. Cond. Matter* **2012**, *24*.

(68) Oster, G.; Riley, D. P. Scattering from cylindrically symmetric systems. *Acta Cryst.* **1952**, *5*, 272–276.

(69) Albouy, P.-A.; Ayral, A. Coupling x-ray scattering and nitrogen adsorption: An interesting approach for the characterization of ordered mesoporous materials. Application to hexagonal silica. *Chem. Mater.* **2002**, *14*, 3391 – 3397.

(70) Zickler, G. A.; Jähnert, S.; Wagermaier, W.; Funari, S. S.; Findenegg, G. H.; Paris, O. Physisorbed films in periodic mesoporous silica studied by in situ synchrotron small-angle diffraction. *Phys. Rev. B* **2006**, *73*.

(71) Rouquerol, J.; Avnir, D.; Fairbridge, C. W.; Everett, D. H.; Haynes, J. M.; Pernicone, N.; Ramsay, J. D. F.; Sing, K. S. W.; Unger, K. K. Recommendations for the characterization of porous solids (IUPAC Technical Report). *Pure Appl. Chem.* **1994**, *66*, 1739–1758.

(72) Kruk, M.; Jaroniec, M.; Sayari, A. Application of large pore MCM-41 molecular sieves to improve pore size analysis using nitrogen adsorption measurements. *Langmuir* **1997**, *13*, 6267–6273.

(73) Landers, J.; Gor, G. Y.; Neimark, A. V. Density functional theory methods for characterization of porous materials. *Coll. Surf. A* **2013**, *437*, 3–32.

(74) Ustinov, E.; Do, D. Application of a generalized thermodynamic approach to characterize mesoporous materials. *Coll. Surf. A* **2006**, *272*, 68–81.

(75) Kruk, M.; Jaroniec, M.; Ko, C.; Ryoo, R. Characterization of the porous structure of SBA-15. *Chem. Mater.* **2000**, *12*, 1961–1968.

(76) Lukens Jr., W. W.; Schmidt-Winkel, P.; Zhao, D.; Feng, J.; Stucky, G. D. Evaluating pore sizes in mesoporous materials: a simplified standard adsorption method and a simplified Broekhoff-de Boer method. *Langmuir* **1999**, *15*, 5403–5409.

(77) Ribeiro Carrott, M.; Candeias, A.; Carrott, P.; Ravikovitch, P.; Neimark, A.; Sequeira, A. Adsorption of nitrogen, neopentane, n-hexane, benzene and methanol for the evaluation of pore sizes in silica grades of MCM-41. *Microp. Mesop. Mater.* **2001**, *47*, 323–337.

(78) Kruk, M.; Jaroniec, M. Gas adsorption characterization of ordered organic-inorganic nanocomposite materials. *Chem. Mater.* **2001**, *13*, 3169–3183.

(79) Neimark, A. V.; Ravikovitch, P. I.; Grün, M.; Schüth, F.; Unge, K. K. Pore size analysis of MCM-41 type adsorbents by means of nitrogen and argon adsorption. *J. Coll. Interf. Sci.* **1998**, *207*, 159–169.

(80) Van Der Voort, P.; Ravikovitch, P.; De Jong, K.; Benjelloun, M.; Van Bavel, E.; Janssen, A.; Neimark, A.; Weckhuysen, B.; Vansant, E. A new templated ordered structure with combined micro- and mesopores and internal silica nanocapsules. *J. Phys. Chem. B* **2002**, *106*, 5873–5877.

(81) Yue, Y. H.; Gédéon, A.; Bonardet, J.-L.; d'Espinose, J. B.; Melosh, N.; Fraissard, J. Direct incorporation of A1 in SBA mesoporous materials: characterization, stability and catalytic activity. *Stud. Surf. Sci. Catal.* **2000**, *129*, 209218.

(82) Gommes, C. J.; Ravikovitch, P.; Neimark, A. Positive curvature effects and interparticle capillary condensation during nitrogen adsorption in particulate porous materials. *J. Coll. Interf. Sci.* **2007**, *314*, 415–421.

(83) Robitzer, M.; Renzo, F. D.; Quignard, F. Natural materials with high surface area. Physisorption methods for the characterization of the texture and surface of polysaccharide aerogels. *Microp. Mesop. Mater.* **2011**, *140*, 9–16.

(84) Everett, D.; Haynes, J. Model studies of capillary condensation. I. Cylindrical pore model with zero contact angle. *J Coll. Interf. Sci.* **1972**, *38*, 125–137.

(85) Nguyen, P. T. M.; Do, D. D.; Nicholson, D. On the cavitation and pore blocking in cylindrical pores with simple connectivity. *J. Phys. Chem. B* **2011**, *115*, 12160–12172.

(86) Schneider, D.; Kondrashova, D.; Valiullin, R. Phase transitions in disordered mesoporous solids. *Scientific Reports* **2017**, *7*, 7216.

Graphical TOC Entry